Cellulose nanocrystal dispersions conjugated with symmetric and asymmetric dialkylamine groups

(article starts on next page)

ORIGINAL RESEARCH

Cellulose nanocrystal dispersions conjugated with symmetric and asymmetric dialkylamine groups

Sylwia Wojno · Amit Kumar Sonker ·
Mohit Garg · Sahana Cooper ·
Mikael Rigdahl · Matthieu Linares ·
Igor Zozoulenko · Roland Kádár ·
Gunnar Westman

Abstract The present study discusses the effect of symmetric and asymmetric grafting on the surface of CNCs (cellulose nanocrystals) on their dispersion properties using dialkyl azetidinium salts. Three dialkylamine of different size and chain length were successfully grafted to the sulfate groups on the surface of CNCs by conjugation of azetidinium salts. The coupling process resulted in the formation of 2-hydroxypropyl-N-dialkylamine conjugated to the CNC sulfate groups abbreviated as C_n-N-C_m-Prop-2-OH-CNC, where m, n are the number of carbons in the alkyl groups, each with a total of $m + n = 12$, with $(m, n) = (11, 1); (9, 3); (6, 6)$. Molecular dynamics simulations were used to assess the probable morphology of the grafted chains and the interaction potential between CNCs. Steady shear simultaneously combined with polarized light imaging and oscillatory shear rheological measurements were used to evaluate for the first time the impact of the CNC surface modifications on their dispersion flow and optical properties. Overall, the results show that the different linker topologies could effectively promote different types of aggregation morphologies based on the size of the linker, their flexibility and their most probable conformation.

Sylwia Wojno, Amit Kumar Sonker, Mohit Garg contributed equally to the work.

S. Wojno · M. Rigdahl · R. Kádár (✉)
Department of Industrial and Materials Science, Division of Engineering Materials, Chalmers University of Technology, SE-412 96 Gothenburg, Sweden
e-mail: roland.kadar@chalmers.se

S. Wojno · A. K. Sonker · M. Garg · I. Zozoulenko (✉)·
R. Kádár · G. Westman (✉)
Wallenberg Wood Science Center (WWSC), Chalmers, Sweden
e-mail: igor.zozoulenko@liu.se

G. Westman
e-mail: westman@chalmers.se

A. K. Sonker · S. Cooper
Department of Chemistry and Chemical Engineering, Division of Chemistry and Biochemistry, Chalmers University of Technology, SE-412 96 Gothenburg, Sweden

A. K. Sonker
Cellulose Films and Coatings, Biomaterial Processing and Products, VTT Technical Research Centre of Finland Ltd. Tietotie 4E, Espoo 02150, Finland

M. Garg · M. Linares
Department of Science and Technology, Laboratory of Organic Electronics, Linköping University, SE-601 74 Norrkoping, Sweden

M. Linares · I. Zozoulenko
Department of Science and Technology, Scientific Visualization Group, Linköping University, SE-SE-601 74 Norrkoping, Sweden

🌊 Springer

Introduction

Cellulose nanocrystals (CNCs) have been highlighted for film applications and as reinforcement in composites (Abitbol et al. 2006, Ferrer et al. 207, Klemm et al. 2011, Salas et al. 2014). To increase the hydrophobicity of their surface, CNCs are usually chemically modified by esterification, alkylation, or silylation of the hydroxyl groups (Klemm et al. 2011, Moon et al. 2011). An alternative method is to use oxidized CNCs with carboxylic acid surface groups and use them as ionic anchors for hydrophobization by trimethylalkyl ammonium salts (Salajková et al. 2012). For modification of the sulfate groups on the CNC surfaces, the only conjugation method published in the scientific literature is by conjugation with azetidinium salts (Börjesson et al. 2018). It has the advantage that it can be easily done in water whereas almost all the hydrophobizations that conjugate to the hydroxyl groups are performed in organic solvents. An additional advantage of conjugation to the sulfate groups is that the thermal stability of CNCs is regained when the acidic sulfate half ester is transformed into a sulfate diester (Börjesson et al. 2018). This is in agreement with investigations by Roman and Winter that showed than an increase in the number of sulfate groups correlated to a reduction in thermal stability (Roman and Winter 2004). A similar effect has been found by Wang et al. (2004) who reported that an inhibited degradation reaction occurs when the hydrogen ion on the sulfate group is replaced by a sodium ion.

Upon self-organization, many of the CNC dispersions show photonic properties. Gray and coworkers (Gray 2016, 2020, Revol et al. 1992) have done pioneering work and showed that CNCs form an isotropic to chiral liquid-crystalline phase transition above a critical concentration upon drying. They have shown that films made from aqueous dispersions of CNCs exhibit a color reflection when illuminated with polarized light and that the color from CNCs is associated with the pitch length between the layers of chiral nematic CNCs (Revol et al. 1998, 1997). They also showed that the pitch length depended upon the size of the counter ion coordinated to the sulphate groups.

Subsequently, it has been demonstrated by others that the color also relies on the size distribution of CNCs (Dumanli et al. 2014a, b), the angle between the layers, and the incident wavelength (Liu et al. 2014). Nevertheless, the described observations have primarily centered on static (microscopic) conditions. Under dynamic conditions, i.e. flow, the nanostructural ordering is dominated by nematic rather than chiral nematic structuring, with a complex interplay between concentration dependent ordered domains and the applied flow-field (Gray 2016, Kádár et al. 2020, Shafiei-Sabet et al. 2012). Specifically, combined rheology - polarized light imaging on aqueous CNC dispersions has focused on the effects of concentration, sonication conditions, degree of sulfation, ionic strength effects, orientation under shear flow (Fazilati et al. 2021, Kádár et al. 2020, Kádár et al. 2021, Shafiei-Sabet et al. 2012, Wojno et al. 2022) and nonlinear rheological response (Wojno et al. 2022, 2023a, b). Microstructural CNC dynamics in shear flow has also been considered using other complementary techniques (Calabrese et al. 2021, Diaz et al. 2013, Ebeling et al. 1999, Haywood et al. 2017). When it comes to hydrophobization, CNCs are typically functionalized using reagents that result in a surface covered with linear alkyl groups. Increased hydrophobicity is generally believed to reduce CNC self-aggregation while enhancing its compatibility with a polymeric matrix (Hasani et al. 2008, Holland and Rubingh 1999). This will also affect the rheological properties of the system. Furthermore, if a uniform organization is formed, similar to liquid crystalline phases, the optical properties of the system will also be influenced.

In this framework, we examine the impact of dialkylamine groups grafted to the sulfate groups. CNCs with reduced amount of sulfate groups were used to obtain CNCs with sulfate groups further apart to minimize intra hydrophobic interactions between alkyl groups on the same CNC crystallites. The three dialkylamine groups in the study had in total 12 carbons. This number was chosen to minimize effects from to strong micelle formation and from earlier work in our lab we have found that when the linkers have 14 or more carbons in the dialkyl segment the CNC suspension starts to phase separate and/or form unstable foams (Nilsson 2017). Given that these dialkylamines possess an equal number of atoms, their total accessible surface area (ASA) and solubility are comparable. However, it's worth noting that the individual alkyl groups exhibit

distinct ASA and van der Waals regions. Supplementary material (Section S1.7 Structure properties) contains the calculated data for reference. The ASA for particular alkyl groups were calculated using DataWarrior software. Molecular modeling was performed to get further insight in how the dialkyl-N-2-hydroxy propyl group was positioned in space and asses their probability distribution, a potential mean force of interaction between nanocrystals. The shear rheological properties and shear-induced optical activity of the modified CNC dispersions were experimentally evaluated. Recently, we have examined the influence of similar surface modifications on the nonlinear rheology of isotropic (non-optically active) gels. However, here we consider for the first time the impact of surface grafting of symmetric and asymmetric alkyl amines on sulfate groups of CNC crystals that show optical activity. In the present work, a direct one step grafting of dialkyl amine on sulfate groups on CNCs is performed. The surface modification of CNCs utilized additives with concentration less than 10 wt% to maintain its biodegradability and crystal structure. There is no conversion of cellulose to other polymorphs like cellulose II upon surface modification. Modified CNC suspensions show promising applications in flexible electronics, photonics, neutral surfactants, functional foams etc.

Materials and methods

Synthesis of amines and azetidinium salts

Dihexyl amine (C_6-N-C_6) was purchased and two other amines, nonyl-propyl amine (C_9-N-C_3) and undecyl-methyl amine (C_{11}-N-C_1) were synthesized by reductive amination of the relevant aldehyde and amine. These amines were used to synthesize the azetidinium salts, 1,1-dihexyl-3-hydroxyazetidin-1-ium chloride, 1-nonyl-1-propyl-3-hydroxy-azetidin-1-ium chloride, 1-methyl-1-undecyl-3-hydroxy-azetidin-1-ium chloride. Further details regarding their synthesis are available in the Sections S1.4.

Isolation of CNCs

The method described by Hasani et al. (2008) was used to manufacture CNCs, with some scale-up adjustments. Here, microcrystalline cellulose (MCC) was acid hydrolyzed with sulfuric acid (64 wt%) to obtain CNC-OSO_3H, which we label in the following as CNCs, for simplicity. The surface charge (-OSO_3^-) in terms of sulfate content was determined by potentiometric titration. Low sulfated CNC suspensions were prepared by autocatalyzed desulfation (Beck and Bouchard 2014) from 2 wt% of highly sulfated CNCs with high sulfate content (345 ± 21 μmol/g). This was achieved by heating to 70°C for 2 hours. Dialysis was performed to remove the formed sulfuric acid. Potentiometric titration was then performed to calculate the sulfate content after desulfation and it was determined to be 160 ± 4 μmol/g. Deionized water (Mili-Q Purification System) was used to dilute suspensions to 1.5 wt%. For further details on the characterization of CNCs such as potentiometric titration, NMR, zeta potential, etc. see Section S1.

Modification of CNCs with azetidinium salts

The CNCs were modified with the three different azetidinium salts, to give C_6-N-C_6- Prop-2-OH-CNC , C_9-N-C_3- Prop-2-OH-CNC, and, C_{11}-N-C_1-Prop-2-OH-CNC. In other words, if m, n are the number of carbons in each alkyl group, each modification had a total of $m + n = 12$, with $(m, n) = (11, 1); (9, 3); (6, 6)$. The ratio of azetidinium salt to CNC dispersion was taken in accordance with a 1÷1 molar ration of sulfate content÷azetidinium salt. Conjugation of azetidinium salts to sulfate half esters was done by keeping the mixture at 90°C for 4 hrs. Upon completion, the mixture was allowed to cool to room temperature. Unreacted azetidinium reagent was removed from the reaction mixture by dialysis(Spectra/Por® molecular porous membrane tubing, MWCO 12-14 kDa) against deionized water for 48 hours. For detailed synthesis and characterization of dialkyl amines and azetidinium salts, see Sections S1.4 - 1.5. The chemical structures are presented in Fig. SI2.

Characterization techniques

Infrared spectra were recorded using a PerkinElmer Spectrum One FT-IR spectrophotometer (Waltham, MA, US) that included an attenuated Total Reflectance (ATR; diamond crystal) attachment (GladiATR) from Pike Technologies. Measurements were conducted at room temperature in air and 32 scans in the range of

4000-400 cm-1 with resolution of 4 cm[1]. The FT-IR data was normalized, and background corrected.

Thermal gravimetrical analysis (TGA) was performed using a TGA/DSC 3 + Star system (Mettler Toledo, Switzerland) to determine the onset temperature for thermal degradation. Samples of 5 mg were weighed out and heated from 25 to 500 °C at a rate of 5 °C/min under a nitrogen flow rate of 20 mL·min[1].

A Zetasizer Nano ZS (Malvern Instruments, UK) was used to measure the zeta-potential for all samples. A 50 mW diode-pumped solid-state laser was used as the light source with a wavelength of 532 nm. The concentration of the test samples was 0.1 wt% and their pH was the same. DTS1070 folded capillary cells were filled with each sample and allowed to stabilize for 120 s, repeated 6 times and the average value was reported. All measurements were conducted at 25 °C.

An Anton Paar MCR 702 Twin Drive rotational rheometer (Graz, Austria) was used for the rheological characterization. All measurements were performed on suspensions containing 1.5 wt% CNCs and the testing temperature was 23°C. Two sets of tests were performed: (i) steady shear and (ii) oscillatory shear tests. Both were performed in single motor - transducer configuration using a custom rheo-optical visualization setup, see Fig. 1. Thus, a parallel plate geometry of $(2 \cdot R =)$43 mm in diameter with a measuring gap of 1 mm was used. The lower and upper plates were made of glass. The outer area of the upper geometry ($L \cong 7.5$ mm in Fig. 1) can be used for visualizations in transmission mode. Two linear polarizers were placed above the upper geometry and below the lower geometry at 90° relative orientation (cross-polarized) for polarized light imaging during flow (Fazilati et al. 2021, Kádár et al. 2021, Mykhaylyk et al. 2016, Völker-Pop 2014). For the steady shear tests, to ensure that steady state was achieved, a custom procedure was applied whereby time-dependent data for each shear rate was acquired manually and later post-processed (Kádár et al. 2020). The steady shear measurements were conducted within a shear rate range of 0.01 to 100 s[1]. Dynamic strain sweeps oscillatory shear tests were also performed. The tests were performed at a constant angular frequency of 2 rad/s with the strain amplitude ranging from 0.01 to 1500%.

Molecular modeling

The nanocrystalline structure of cellulose was generated by placing the cellulose chains in a I_β crystal lat-
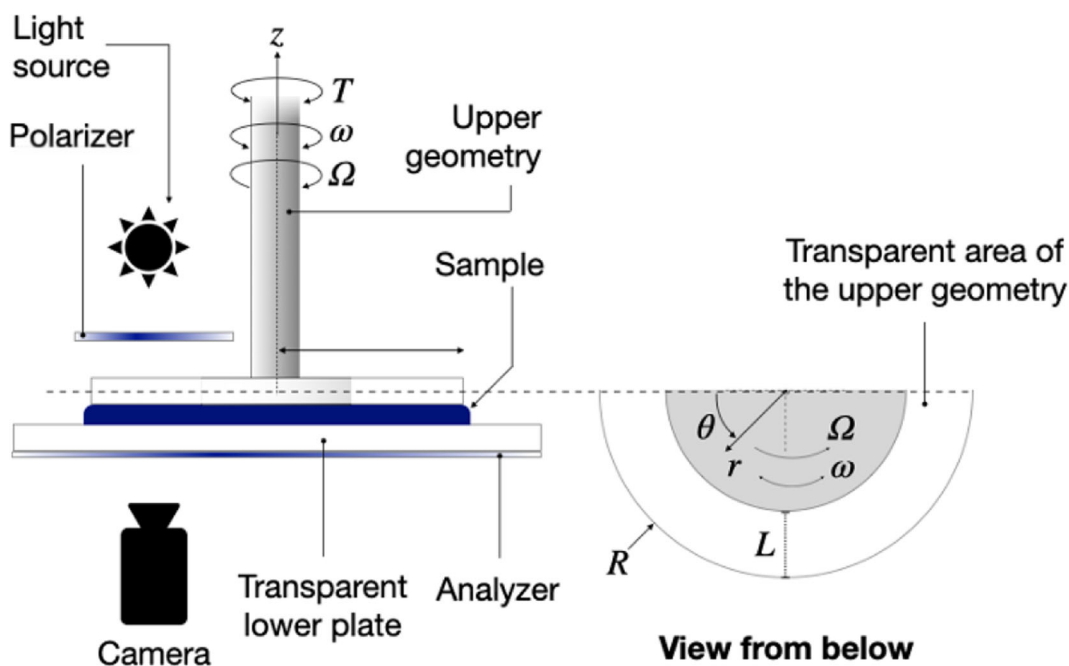

Fig. 1 Schematic representation of the combined rheology-polarized light optical visualization setup used in the study ($L \cong 7.5$ mm)

tice using cellulose builder toolkit (Gomes and Skaf 2012). The sulfonation and grafting of azetidinium (Az) salts on the nanoparticle surface were done using Avogadro (Hanwell et al. 2012). OPLS-AA force field (Jorgensen et al. 1996) extended for carbohydrates was used for CNCs and their grafts. A TIP3P water model was used in the study (Jorgensen et al. 1983). Two types of Molecular Dynamics (MD) calculations were performed (details in Section S2, Molecular modeling). First, the morphology of grafted salts on the CNC surface was studied, then the change in the free energy between two CNCs and between two nematic planes formed by CNC aggregation, with and without the grafted substituents, was calculated.

Substituent morphology on CNC surfaces

The CNC surface was generated by placing the cellulose chain in a rectangular cross-section of 9.4×5.8 nm^2 with a thickness of 1.5 nm, which is formed by 36 chains of cellulose stacked in 2 layers in (010) plane as shown in Fig. SI 9(a, b). A cellulose with a chain length of 12 glucose units was used for this calculation across the periodic box to simulate an infinite surface of CNCs with the propyl-2-hydroxy-dialkyl groups grafted on it. A degree of surface substitution (DSS), defined as the ratio of modified hydroxyl groups to the total hydroxyl groups, of 0.07 was chosen in the calculations to ensure that alkyl groups adjacent to each other on the CNC surface did not start to interact with each other. A limit for the interaction of adjacent dialkyl groups was found at DSS = 0.02. Further details on DSS, simulation parameters and how variation in DSS affected the linker surface distribution probability are given in the Section S2.1.

Free energy between CNCs

The CNC crystals built consist of cellulose I_β with 18 chains arranged in a hexagonal cross-section with dimensions of 3.2×3.5 nm^2 and length of 8.3 nm. The CNC crystal has three face types, (100), considered as a hydrophobic surface, and (110) and (1-10) considered as hydrophilic surfaces, as shown in Fig. SI 9. Three types of contact arrangements formed by relative orientations of faces of these nanocrystals: (100)-(100), (100)-(1-10) and (110)-(110) were considered.

The change in the free energy (the potential of mean force, PMF) between the two CNCs, governed by van der Waals and electrostatic interactions, was calculated as a function of the separation distance. The effect of linkers on hydrophobic phenomena was simulated through potential by mean force which differed depending on the grafted symmetric or asymmetric chains. The procedure to calculate PMF and simulation details is described in the Section S2 (Molecular modeling).

Results and discussion

Chemical modification verified by FT-IR

Figure 2 shows the FT-IR spectra for the untreated and modified CNC samples. The first derivative of transmittance with respect to the wavenumber. All four samples gave the expected signals for cellulose (Mykhaylyk 2010). There is a broad band of signals at 3600-3000 cm^{-1} which is known to correspond to the -OH group on cellulose. The peak at 3000-2900 cm^{-1} for all the samples is caused by the aliphatic C-H bonds on cellulose and the grafted propyl-2-hydroxy-dialkyl chains. The C-O-C bond between each glucose unit is represented by the peak at 901 cm^{-1} while the peak at 1640 cm^{-1} is caused by water which has been absorbed onto the cellulose. Looking closer at the width and height of the peak at 3000-2900 cm^{-1} for the untreated CNC sample, it is evident they are different from the functionalized CNCs. The modified samples exhibited a stronger peak at approximately 2850 cm^{-1} the CH$_2$-groups, which is expected since upon modification the number of CH$_2$-groups is increased (Fig. 2c). Furthermore, the peak at 814 cm^{-1} for the untreated CNCs was shifted to 808 cm^{-1} for the modified samples (Fig. 2b and reaction scheme SI2). These peaks correspond to the C-O-S found on the sulfate half ester and diester (Chen et al. 2013). It should be stressed that these signals are very weak since it is a very small percentage of the total number of glucose units in the sample that have sulfate groups. Thus, not a strong intensity but a small shift in this region is a strong indication of successful modification of CNCs with azetidinium salt. Additionally, the expected changes in the 2800-2950 cm^{-1} region for the CH$_2$ and CH$_3$ vibrations are also difficult to detect. By taking the derivative of the signals the change in this region becomes clearer, see Fig. 2c.
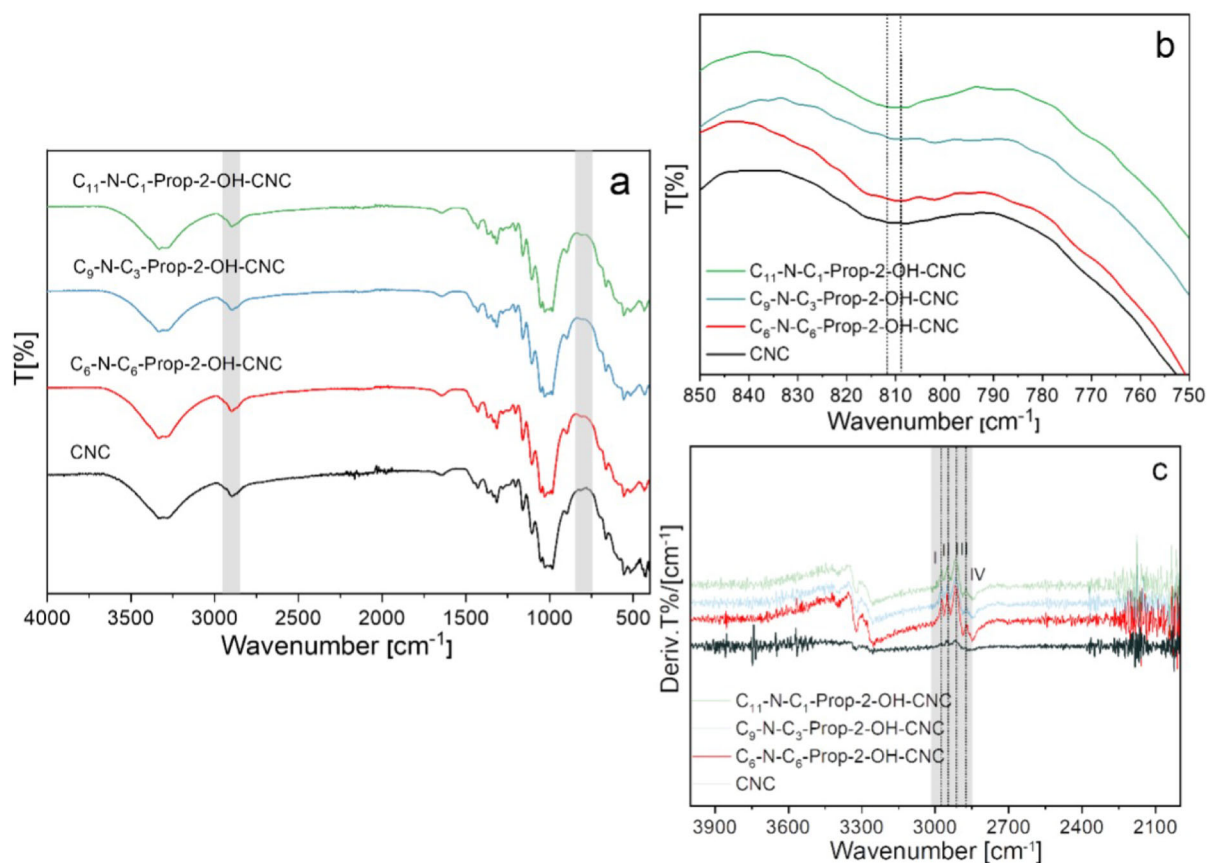
Fig. 2 (a) Full range FTIR of CNCs and surface modified CNCs. (b) FTIR spectra from 850-750 cm^{-1} (highlighted in grey) indicates shift for C-O-S for modified CNCs samples from 814 to 808 cm-11 in comparison to untreated CNC samples. (c), FTIR spectra from 4000 to 2000 cm^{-1} particularly, first derivative of

the alkyl band (highlighted in grey). The short, dashed lines, I, II, III and IV corresponds to -CH$_3$ (anti symmetric stretch at 2970-2950 cm^{-1}), CH$_2$ (anti symmetric stretch at 2940-2915 cm^{-1}), -CH$_2$ (symmetric stretch at 2870-2840 cm^{-1}) and -CH$_3$ (symmetric stretch at 2885-2860 cm^{-1}), respectively

Thermal analysis and Zeta-potential (ζ)

The success of the chemical modification was also confirmed via TGA measurements. Figure 3a, b shows the thermal degradation curves resulting from TGA measurements. A significant improvement in thermal stability is seen for the samples modified with azetidinium salts. Table 1 shows that untreated CNCs started to degrade at 150 °C, whereas the modified CNCs had an onset temperature for degradation almost 100 °C higher. The improvement seen here in thermal stability is important for industrial applications, as typical processing temperatures for polymers are much higher than onset temperature seen here for untreated CNCs (Forsgren et al. 2019). The other interesting

characteristic of the TGA curves are the two regions that can be identified. The first, more rapid, weight loss is caused by the acid-catalyzed pyrolysis reaction by the sulphate groups (Wang et al. 2004). The second region is a charring process of the remaining solid material (Roman and Winter 2004). The residual char left at the end of each TGA measurement is given in Table 1.

Zeta-potential (ζ) measurements, see Table 1, show that surface modification did not chance colloidal stability, see Table 1 and Fig. SI 3-5. Furthermore, the ζ-potential was independent of surface modification. This is in contrast to a previous report on similar surface grafted CNCs by Forsgren et al. (2019), where the ζ-potential decreased significantly after surface grafting. The discrepancy can be attributed to differences
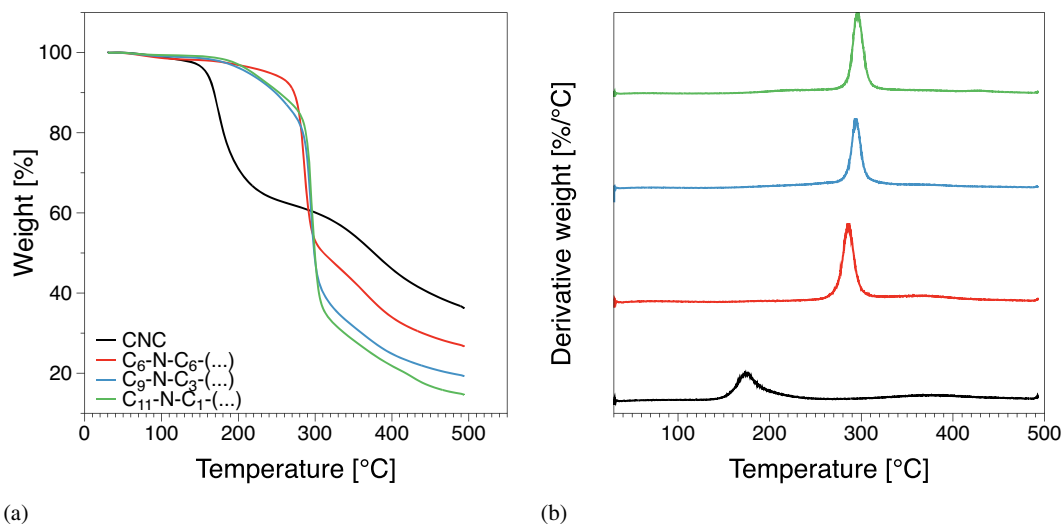
Fig. 3 (a) TGA and (b) DTGA curves showing thermal degradation of untreated and modified CNC samples

in the sulfate content of the CNCs after autocatalyzed desulfation.

Molecular dynamics studies

In order to gain a better understanding of the cellulose surface functionalized with the dialkylamine segments and their interaction, molecular dynamics (MD) simulations of the surface grafted CNCs were performed, as illustrated in Fig. 4(a)-(c). The determined angular probability distributions of the different branches of the alkyl chains can be found in Fig. 4(d)-(f) (DSS = 0.07). The angular distribution from MD simulations and probability distribution for other angles can be found in Figs. SI4 - SI6. The MD simulations show that for C_6-N-C_6-Prop-2-OH-CNC, which presents two similar alkyl chains of six carbons, the probability distribution is broader and not as far out from the surface,

i.e. an oblate ellipsoid distribution, Fig. 4(f). However, for the C_{11}-N-C_1-Prop-2-OH-CNC, the most asymmetric dialkyl amine, the probability distribution was further away from the surface but not as broad, i.e. a prolate ellipsoid distribution, Fig. 4(d). Based on force field calculations, it has also been similarly suggested that linear molecules elongate and form a prolate ellipsoid structures while branched molecules form oblate ellipsoids (Eisenriegler and Bringer 2007, Shah et al. 2005). The same appears to be true for the present study, considering that the C_6-N-C_6-Prop-2-OH-CNC can be seen as a more branched unit (Fig. SI4), whereas the C_{11}-N-C_1-dialkyl can be considered as a more linear substituent. Those differences observed in the distribution illustrate how the nature of the different dialkyl chains structure can affect CNC surface topology. For the 11-N-1 linker the 2-hydroxy-propyl fragment has a tilt angle of 30°, Fig. 4(d), whereas for the C_6-N-C_6 the linker has a tilt angle of 60°, Fig. 4(f).

Table 1 Onset temperature for thermal degradation, residual char content and zeta-potential for untreated and modified CNCs

Sample name	T_{degr} [°C]	T_{decomp} [°C]	Residual char [wt%]	ζ [mV]
Untreated CNCs	150	178	36	-33.2 ± 0.24
C_6-N-C_6-Prop-2-OH-CNC	263	287	26	-34 ± 1.2
C_9-N-C_3-Prop-2-OH-CNC	270	295	19	-33.4 ± 0.6
C_{11}-N-C_1-Prop-2-OH-CNC	270	295	16	-35.8 ± 1

T_{degr} and T_{decomp} are the degradation and decomposition temperatures of the CNCs and modified CNC samples
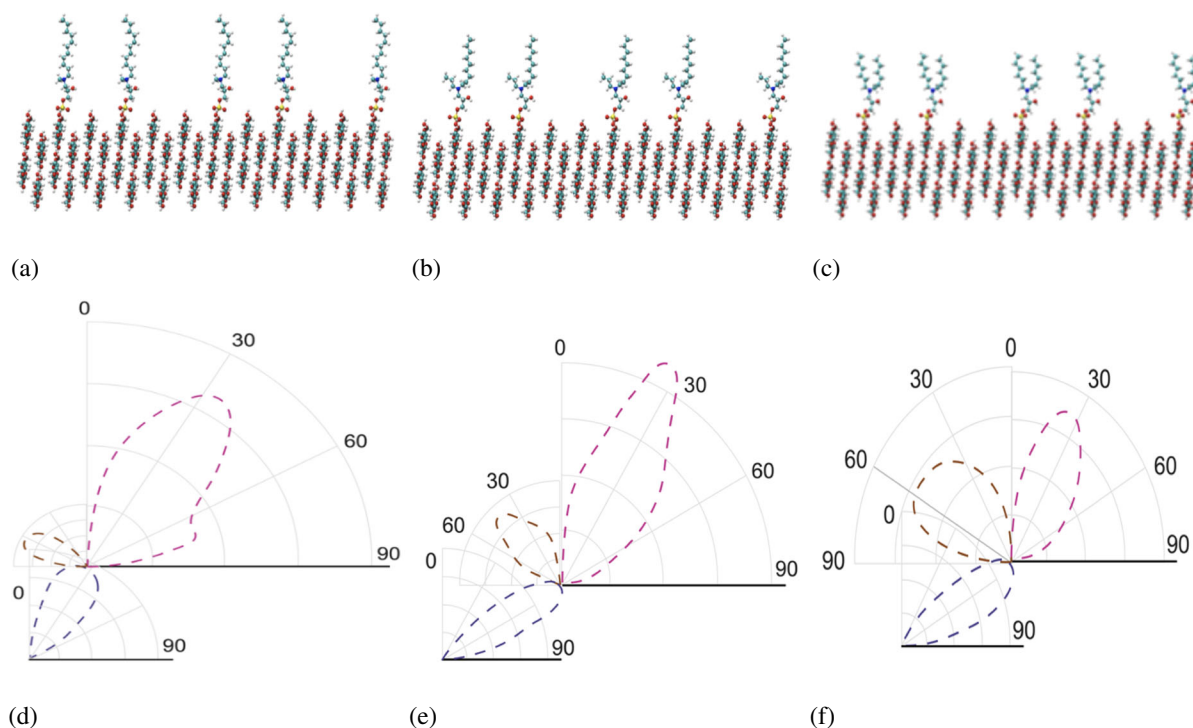
Fig. 4 (a-c) Snapshots of CNCs modified with different type of Az salts. (d-f) Polar plots showing the probability angle distribution of different segments of the linkers of Az salts normal to the nanoparticle surface for DSS=0.07. The lower-left angle distribution (purple colour), in (d)-(f) represents the Prop-2-OH-CNC fragment for reference and the two upper globes (red colour) represent the two alkyl groups. (d) C_{11}-N-C_1-Prop-2-OH-CNC, (e) C_9-N-C_3-Prop-2-OH-CNC, (f) C_6-N-C_6-Prop-2-OH-CNC

The distribution suggests that short chain of the C_{11}-N-C_1-Prop-2-OH-CNC (methyl group) can be quite close to the surface of the CNCs, whereas the long 11-carbon chain has a greater flexibility and points away from the surface. This scenario would allow for a stronger interdigitation of the alkyl chains meaning that more energy would be needed to break up the intermolecular interaction of the C_{11}-N-C_1 chains. In contrast, in C_9-N-C_3-Prop-2-OH-CNC, the short part of the chains is now made of three carbons and would interact more strongly with the CNC surface than the methyl group in C_{11}-N-C_1-Prop-2-OH-CNC provoking a tilt of the 9-carbon chain with respect to the normal of the surface. For C_6-N-C_6-Prop-2-OH-CNC the interdigitation of the chains would be even weaker as a result. However, assuming a partial interdigitation between the 11-carbon chain, this would result in less interaction strength but would promote greater interconnectivity between CNCs, not only because the distances between CNCs would be slightly larger, but also because of the greater flexibility of 11-carbon chains. In contrast, the smaller sized branched linkers could lead to more agglomeration since the CNCs would make contact in closer proximity, potentially promoting a higher strength of interaction. The potential of mean force results, as determined considering the 100-100 contact surfaces, could suggest a different scenario in terms of strenght of interaction. For very low separations, Fig. 5, the strength of interaction for C_6-N-C_6-Prop-2-OH-CNC was higher than for C_9-N-C_3-Prop-2-OH-CNC which in turn was higher than for C_{11}-N-C_1-Prop-2-OH-CNC. However, as the separation distance increases, the level of interaction between the nanocrystals is at first similar, before, above ≈ 10 Å starting to converge towards the untreated CNCs. In addition to this, the differences in the interactions between two untreated CNCs as a function of separation distance are presented in Fig. SI7. The results
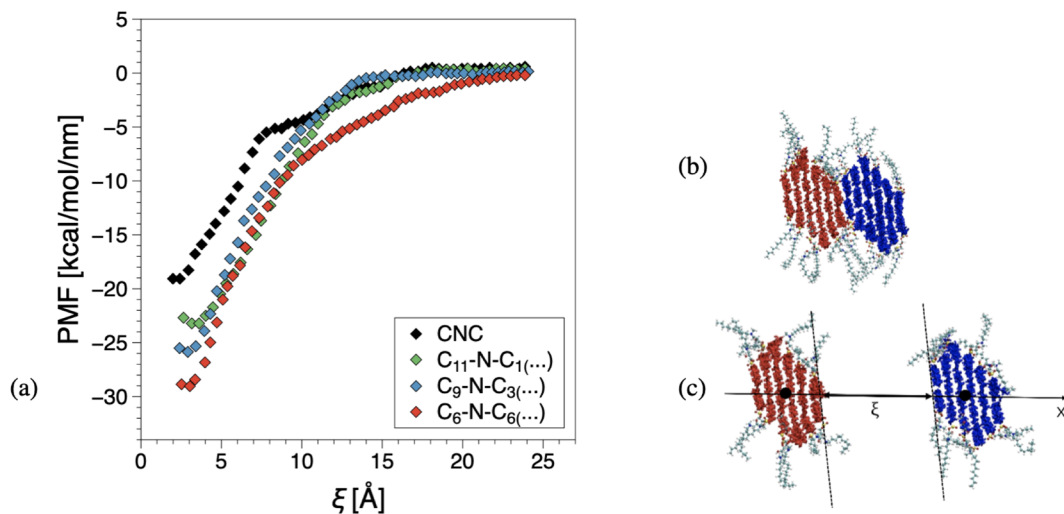
Fig. 5 (a) Potential of mean force (PMF) per unit length of CNCs modified with different type of Az salts as function of surface-to-surface separation distance (ζ) between the CNCs for DSS = 0.07 and for different types of alkyl chains attached to CNCs. The 100-100 contact surfaces were considered while calculating the PMF. The initial and final configuration of CNCs during PMF calculation are shown in (b) and (c) respectively. The distance ξ corresponds to the minimum separation distance in the x-direction between the outermost hydrogen atoms at 100 surfaces as indicated in the figure, where the x-direction goes between the centers of the mass of two CNC crystals. (The centers of the mass are marked by filled circles in (c)

support the Lindman hypothesis, that van der Waals intearctions of cellulose may outweigh hydrogen bonding (Glasser et al. 2012, Wohlert et al. 2022).

It should be noted that this is modelled without effects from shear or close-packed nanocellulose particles. There, additionally, alkyl chain aggregation from neighboring crystallites and flow induced tilt of the dialkylamine group towards the crystallite surface when they start to become closer to each other, may occur. However, we can consider the molecular modeling as limiting ideal cases that could be considered as a reference for interpreting the flow results.

Rheology and shear-induced polarized light imaging

The steady shear viscosity functions of the samples are compared in Fig. 6. All azetidinium salt modifications resulted in at one order of magnitude increase in shear viscosity compared to untreated CNC dispersions, similar to previous findings (Sahlin et al. 2018). Due to the low viscosity of untreated CNCs (low torques), the first few points at shear rates < 1 1/s were cut for this sample. The general variation in viscosity magnitude was CNC < C_6-N-C_6-Prop-2-OH-CNC < C_9-N-C_3-Prop-2-OH-CNC < C_{11}-N-C_1-Prop-

2-OH-CNC. At the highest shear rates, where a strong orientation of the constituents in the flow direction is expected, the viscosity functions appear to converge (Derakhshandeh et al. 2013, Kádár et al. 2020).

Figure 7 shows polarized light imaging (PLI) results taken during the steady shear data in Fig. 6. Shear rate
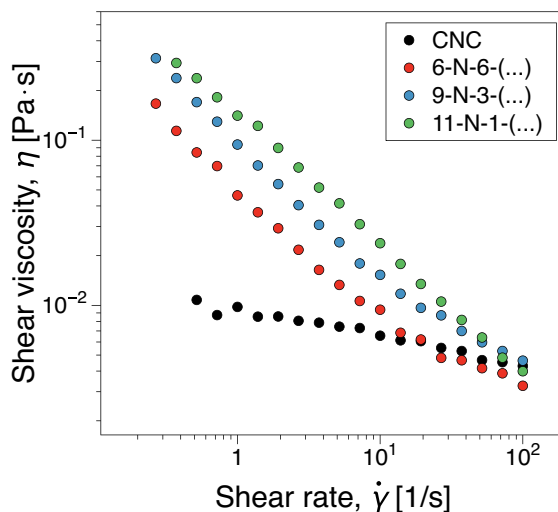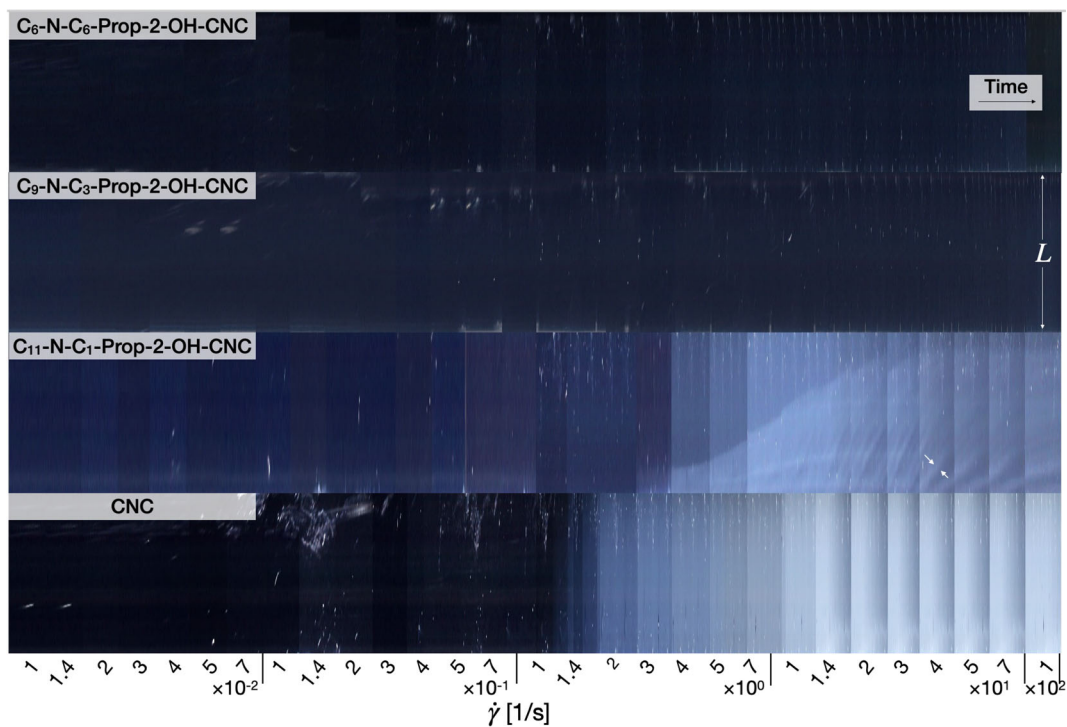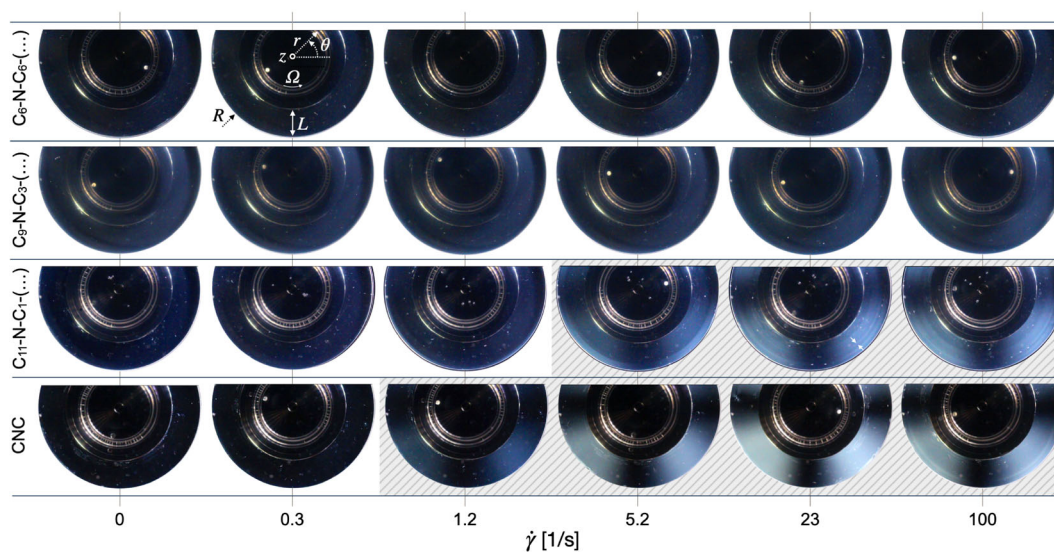

Fig. 6 Shear viscosity functions from steady shear tests for samples at 1.5 wt%

(a)

(b)

Fig. 7 (a) Space-time diagrams of the birefringence pattern development during the steady shear tests in Fig. 6 for samples at 1.5 wt%. (b) Still frame visualizations at selected shear rates. Gray hatched regions highlight visualizations where a Maltese-cross pattern could be distinguished. The white arrows mark ripples that could be associated to secondary flows

intervals in the space-time diagrams, Fig. 7(a), have been re-scaled to be equidistant. This is to compensate for the fact that lower shear rates require significantly more time to reach steady state. For reference, individual frames out of the PLI video recordings, where the Maltese-cross pattern can be directly observed, are shown at selected shear rates in Fig. 7 (b). The Maltese-cross pattern, observed (for cross-polarized setups) in the form of alternating dark and light colored regions, see the images in Fig. 7(b) (hatched regions), signifies the general orientation of optical indicatrices in the flow direction (Mykhaylyk 2010). The dark shades (extinction) appear when one of the refractive indices of the optical indicatrices is parallel to the incident polarization direction. The azimuthal angle of line L (see angle θ in Fig. 7(b)) used to construct the space-time diagrams was chosen so that it captures the onset of the so-called Maltese-cross pattern. Thus, the onset of the Maltese-cross pattern in the space-time diagrams in Fig. 7(a) can be observed in the form of light colored regions. Note that the concept of optical indicatrix does not imply what lengthscales in the sample are oriented in the flow direction to create birefringence. This means that the tests cannot evidence whether the oriented structures are individual CNCs, bundles or other form of agglomerates. Since both in flow and static conditions a rotation of the relative polarizer/analyzer angle did not result in any brightly colored areas (Kádár et al. 2021), we assign the onset of birefringence to the orientation of nanocrystals or aggregates thereof in the flow direction (Hausmann 2018) and not to any form of self-assembly. Thus, as all test samples are assumed to be in a randomly oriented state at the beginning of shear, whether or not birefringence occurs and at what shear rates, can be interpreted as the ability of the CNC structure to uniformly orient in the flow direction resulting in optically anisotropic properties at the scale of observation. For the untreated CNCs, the Maltese-cross pattern was detected at $\dot{\gamma} \cong 1$ 1/s. For the modified CNCs, C_{11}-N-C_1-Prop-2-OH-CNC was the only sample that exhibited birefringence, above $\dot{\gamma} \cong 4$ 1/s, in the investigated shear rate range. In addition, the suspension likely exhibits a form of flow instability as evidenced by the periodic ripples forming from the outer edge of the geometry, where the shear rates are highest, see the white arrows in Fig. 7(a) and the corresponding periodic rings for C_{11}-N-C_1-Prop-2-OH-CNC at $\dot{\gamma} \geq 23$ 1/s in Fig. 7(b). In contrast, the addition of symmetric alkyl chains, i.e. C_6-N-C_6-Prop-2-OH-CNC, resulted

in a total suppression of shear-induced birefringence in the investigated shear rate range.

From strain sweep tests, Fig. SI8, in contrast to the untreated CNC dispersions that showed a liquid-like behavior ($G' < G''$), all surface treated dispersions showed a gel-like behavior ($G' > G''$) as well some level of weak strain overshoot (WSO). WSO refers to the local maximum in the loss modulus, G'', at the transition to the nonlinear region in strain sweep tests. From microstructural point of view, a weak strain overshoot behavior has been associated to microstructural jamming followed by yielding (Derakhshandeh et al. 2013). This effect appears nearly absent for C_6-N-C_6-Prop-2-OH-CNC. At the same time C_{11}-N-C_1-Prop-2-OH-CNC showed arguably the most pronounced WSO behavior, Fig. 6. This would be in agreement with the higher steady shear viscosities recorded, as both tests include weakly nonlinear / nonlinear conditions.

Considering all the data in the context of the MD simulations, one microstructural scenario could be that the different linker topologies could effectively promote different types of aggregation morphologies based on the size of the linker, their flexibility and their most probable conformation. Thus, longer linkers would promote highly interconnected networks whereas more branched (shorter) structures would promote network morphologies dominated by more packed agglomerates. This would effectively limit the number of connection points between the agglomerates in the gel network. In such a scenario, the viscosity data and the WSO in strain sweep would be interpreted as a measure of the inter-connectivity of formed CNC networks. Furthermore, the absence of birefringence would confirm that whatever aggregates are present in the more branched topologies, C_6-N-C_6-Prop-2-OH-CNC and C_6-N-C_3-Prop-2-OH-CNC, and are distorted by the flow at high shear rates, they do not show any measurable optical anisotropy. In contrast, linear topologies with their more flexible linkers would facilitate a preferential orientation in the flow direction of the broken network at high shear rates leading to shear induced birefringence. While this does not exclude the presence of aggregates, however, it does suggest that the resulting nanostructure possesses sufficient anisotropy that once oriented in the flow direction results in birefringence. Referring back to the MD simulations, the scenario outlined could imply that linker-linker connection between the linear linkers may just occur without their complete interdigitation. In terms

of the PMF calculations, the results could suggest that the configuration considered may not be fully representative of the interparticle interactions occurring in the experiments. Relating the molecular dynamics simulations to the rheological data is not straightforward due to the different lengthscales as well as the static vs. dynamic (flow) conditions probed. However, understanding CNC-CNC interactions provides a molecular basis for interpreting the rheological and rheo-optical data.

Conclusions

The surface of cellulose nanocrystals (CNCs) was successfully modified by attaching three distinct dialkylamines through the conjugation of azetidinium salts to sulfate groups. A significant influence of surface modification topology was shown on their self-organization assisted by shear flow. We base the interpretation of the experimental results on molecular dynamics simulations, noting that several hypotheses could be made therefrom. Based on the experimental results, it would appear that, the simulated preferred conformations of the surface grafted linkers and their flexibility play a central role in relating all experiments presented. Thus, linear linker topologies seem to promote a highly interconnected morphology through the linkers' mobility and partial interdigitation and this could be responsible for the higher shear viscosities and weak strain overshoot and the onset of shear-induced birefringence. Branched surface linkers would conversely form distorted aggregate dominated networks with few connections points in-between resulting in smaller viscosities, nearly absent weak strain overshoot and absence of shear induced birefringence. Thus, the results emphasize that when considering the hydrophobization of CNC-derivates, the structure and branching of the constituents must be taken into consideration, since the structure of the alkyl group will affect the rheological and optical properties, as well as flow-induced structuring. Or putting it another way, branching of the alkyl group(s) is a complementary methodology to achieve desired physical properties and interactions. Therefore, the main highlight of the study is that the strength of interaction, mobility and dynamic self-organization can be tailored by surface modification in CNC dispersions.

Compliance with Ethical Standards

Ethics approval and consent to participate Not applicable

Consent for publication Not applicable

Competing interests The authors declare no competing interests.

References

Abitbol T, Rivkin A, Cao Y, Nevo Y, Abraham E, Ben-Shalom T, Lapidot S, Shoseyov O (2016) Nanocellulose, a tiny fiber with huge applications. COBIOT 39:76–88. https://doi.org/10.1016/j.copbio.2016.01.002

Beck S, Bouchard J (2014) Auto-catalyzed acidic desulfation of cellulose nanocrystals. NPPRJ 29(1):6–14. https://doi.org/10.3183/npprj-2014-29-01-p006-014

Börjesson M, Sahlin K, Bernin D, Westman G (2018) Increased thermal stability of nanocellulose composites by functionalization of the sulfate groups on cellulose nanocrystals with azetidinium ions. J Appl Polym Sci 135(10):45963. https://doi.org/10.1002/app.45963

Calabrese V, Haward SJ, Shen AQ (2021) Effects of shearing and extensional flows on the alignment of colloidal rods. Macromolecules 54(9):4176–4185. https://doi.org/10.1021/acs.macromol.0c02155

Chen G, Zhang B, Zhao J, Chen H (2013) Improved process for the production of cellulose sulfate using sulfuric acid/ethanol solution. Carbohydr Polym 95(1):332–7. https://doi.org/10.1016/j.carbpol.2013.03.003

Derakhshandeh B, Petekidis G, Shafiei Sabet S, Hamad WY, Hatzikiriakos SG (2013) Ageing, yielding, and rheology of nanocrystalline cellulose suspensions. J Rheol 57(1):131–148. https://doi.org/10.1122/1.4764080

Diaz JA, Wu X, Martini A, Youngblood JP, Moon RJ (2013) Thermal expansion of self-organized and shear-oriented cellulose nanocrystal films. Biomacromolecules 14(8):2900–2908. https://doi.org/10.1021/bm400794e

Dumanli AG, van der Kooij HM, Kamita G, Reisner E, Baumberg JJ, Steiner U, Vignolini S (2014) Digital color in cellulose nanocrystal films. ACS Appl Mater Interfaces 6(15):12302–12306. https://doi.org/10.1021/am501995e

Dumanli AG, Kamita G, Landman J, van der Kooij HM, Glover BJ, Baumberg JJ, Steiner U, Vignolini S (2014) Controlled, bio-inspired self-assembly of cellulose-based chiral reflectors. Adv Opt Mater 2(7):646–650. https://doi.org/10.1002/adom.201400112

Ebeling T, Paillet M, Borsali R, Diat O, Dufresne A, Cavaillé J-Y, Chanzy H (1999) Shear-induced orientation phenomena in suspensions of cellulose microcrystals, revealed by small angle x-ray scattering. Langmuir 15(19):6123–6126. https://doi.org/10.1021/la990046+

Eisenriegler E, Bringer A (2007) Polymer depletion profiles around nonspherical colloidal particles. J Chem Phys 127(3):034904. https://doi.org/10.1063/1.2751193

Fazilati M, Ingelsten S, Wojno S, Nypelö T, Kádár R (2021) Thixotropy of cellulose nanocrystal suspensions. J Rheol 65(5):1035–1052. https://doi.org/10.1122/8.0000281

Ferrer A, Pal L, Hubbe M (2017) Nanocellulose in packaging: advances in barrier layer technologies. Ind Crops Prod 95:574–582. https://doi.org/10.1016/j.indcrop.2016.11.012

Forsgren L, Sahlin-Sjövold K, Venkatesh A, Thunberg J, Kádár R, Boldizar A, Westman G, Rigdahl M (2019) Composites with surface-grafted cellulose nanocrystals (CNC). J Mater Sci 54:3009–3022. https://doi.org/10.1007/s10853-018-3029-2

Glasser WG, Atalla RH, Blackwell J, Malcolm Brown R, Burchard W, French AD, Klemm DO, Nishiyama Y (2012) About the structure of cellulose: debating the Lindman hypothesis. Cellulose 19(3):589–598. https://doi.org/10.1007/s10570-012-9691-7

Gomes TCF, Skaf MS (2012) Cellulose-builder: a toolkit for building crystalline structures of cellulose. J Comput Chem 33(14):1338–1346. https://doi.org/10.1002/jcc.22959

Gray D (2016) Recent advances in chiral nematic structure and iridescent color of cellulose nanocrystal films. Nanomaterials (Basel) 6(11). https://doi.org/10.3390/nano6110213

Gray DG (2020) Cellulose nanocrystal research; a personal perspective. Carbohydr Polym 250:116888. https://doi.org/10.1016/j.carbpol.2020.116888

Hanwell MD, Curtis DE, Lonie DC, Vandermeersch T, Zurek E, Hutchison GR (2012) Avogadro: an advanced semantic chemical editor, visualization, and analysis platform. J Cheminform 4(1):17. https://doi.org/10.1186/1758-2946-4-17

Hasani M, Cranston ED, Westman G, Gray DG (2008) Cationic surface functionalization of cellulose nanocrystals. Soft Matter 4:2238–2244. https://doi.org/10.1039/B806789A

Hausmann MK, Rühs PA, Siqueira G, Läuger J, Libanori R, Zimmermann T, Studart AR (2018) Dynamics of cellulose nanocrystal alignment during 3D printing. ACS Nano 12(7):6926–6937. https://doi.org/10.1021/acsnano.8b02366

Haywood AD, Weigandt KM, Saha P, Noor M, Green MJ, Davis VA (2017) New insights into the flow and microstructural relaxation behavior of biphasic cellulose nanocrystal dispersions from RheoSANS. Soft Matter 13:8451–8462. https://doi.org/10.1039/C7SM00685C

Holland PM, Rubingh DN (1999) Mixed surfactant systems, chapter 1. American Chemical Society

Jorgensen WL, Chandrasekhar J, Madura JD, Impey RW, Klein ML (1983) Comparison of simple potential functions for simulating liquid water. J Chem Phys 79(2):926–935. https://doi.org/10.1063/1.445869

Jorgensen WL, Maxwell DS, Tirado-Rives J (1996) Development and testing of the OPLS all-atom force field on conformational energetics and properties of organic liquids. J Am Chem Soc 118(45):11225–11236. https://doi.org/10.1021/ja9621760

Kádár R, Fazilati M, Nypelö T (2020) Unexpected microphase transitions in flow towards nematic order of cellulose nanocrystals. Cellulose 27(4):2003–2014. https://doi.org/10.1007/s10570-019-02888-x

Kádár R, Spirk S, Nypelö T (2021) CeLlulose nanocrystal liquid crystal phases: progress and challenges in characterization using rheology coupled to optics, scattering, and spectroscopy. ACS Nanon. https://doi.org/10.1021/acsnano.0c09829

Klemm D, Kramer F, Moritz S, Lindström T, Ankerfors M, Gray D, Dorris A (2011) Nanocelluloses: a new family of nature-based materials. Angew Chem Int Ed Engl 50:5438–66. https://doi.org/10.1002/anie.201001273

Liu D, Wang S, Ma Z, Tian D, Gu M, Lin F (2014) Structure-color mechanism of iridescent cellulose nanocrystal films. RSC Advances 4:39322–39331. https://doi.org/10.1039/C4RA06268J

Moon RJ, Martini A, Nairn J, Simonsen J, Youngblood J (2011) Cellulose nanomaterials review: structure, properties and nanocomposites. Chem Sov Rev 40(7):3941–3994. https://doi.org/10.1039/C0CS00108B

Mykhaylyk OO (2010) Time-resolved polarized light imaging of sheared materials: application to polymer crystallization. Soft Matter 6(18):4430–4440. https://doi.org/10.1039/C0SM00332H

Mykhaylyk OO, Warren NJ, Parnell AJ, Pfeifer G, Laeuger J (2016) Applications of shear-induced polarized light imaging (SIPLI) technique for mechano-optical rheology of polymers and soft matter materials. J Polym Sci Part B: Polym Phys 54(21):2151–2170. https://doi.org/10.1002/polb.24111

Nilsson R (2017) Study of cellulose nanocrystal modification and PLA cellulose nanocrystal composites. Master thesis

Revol JF, Godbout LJ, Gray DG (1998) Solid self-assembled films of cellulose with chiral nematic order and optically variable properties. vol 24

Revol J-F, Bradford H, Giasson J, Marchessault R, Gray D (1992) Helicoidal self-ordering of cellulose microfibrils in aqueous suspension. Int J Biol Macromol 14(3):170–172. https://doi.org/10.1016/S0141-8130(05)80008-X

Revol J-F, Godbout DL, Gray D (1997) Solidified liquid crystals of cellulose with optically variable properties. U.S. Patent 5(629):055

Roman M, Winter WT (2004) Effect of sulfate groups from sulfuric acid hydrolysis on the thermal degradation behavior of bacterial cellulose. Biomacromolecules 5(5):1671–1677. https://doi.org/10.1021/bm034519+

Sahlin K, Forsgren L, Moberg T, Bernin D, Rigdahl M, Westman G (2018) Surface treatment of cellulose nanocrystals (CNC): effects on dispersion rheology. Cellulose 25(1):331–345. https://doi.org/10.1007/s10570-017-1582-5

Salajková M, Berglund LA, Zhou Q (2012) Hydrophobic cellulose nanocrystals modified with quaternary ammonium salts. J Mater Chem 22:19798–19805. https://doi.org/10.1039/C2JM34355J

Salas C, Nypelö T, Rodriguez-Abreu C, Carrillo C, Rojasv OJ (2014) Nanocellulose properties and applications in colloids and interfaces. COCIS 19(5):383–396. https://doi.org/10.1016/j.cocis.2014.10.003

Shafiei-Sabet S, Hamad WY, Hatzikiriakos SG (2012) Rheology of nanocrystalline cellulose aqueous suspensions. Langmuir 28(49):17124–17133. https://doi.org/10.1021/la303380v

Shah D, Fytas G, Vlassopoulos D, Di J, Sogah D, Giannelis EP (2005) Structure and dynamics of polymer-grafted clay suspensions. Langmuir 21(1):19–25. https://doi.org/10.1021/la049857q

Völker-Pop L (2014) Optical methods in rheology: polarized light imaging. Chem Listy 108:697–724

Wang N, Ding E, Cheng R (2004) Thermal degradation behaviors of spherical cellulose nanocrystals with sulfate groups. Polymer 48(12):3486–3493. https://doi.org/10.1016/j.polymer.2007.03.062

Wohlert M, Benselfelt T, Wågberg L, Furó I, Berglund LA, Wohlert J (2022) Cellulose and the role of hydrogen bonds: not in charge of everything. Cellulose 29(1):1–23. https://doi.org/10.1007/s10570-021-04325-4

Wojno S, Fazilati M, Nypelö T, Westman G, Kádár R (2022) Phase transitions of cellulose nanocrystal suspensions from nonlinear oscillatory shear. Cellulose 29(7):3655–3673. https://doi.org/10.1007/s10570-022-04474-0

Wojno S, Ahlinder A, Altskär A, Stading M, Abitbol T, Kádár R (2023) Percolation and phase behavior in cellulose nanocrystal suspensions from nonlinear rheological analysis. Carbohydr Polym 308:120622. https://doi.org/10.1016/j.carbpol.2023.120622

Wojno S, Sonker AK, Feldhusen J, Westman G, Kádár R (2023) Isotropic gels of cellulose nanocrystals grafted with dialkyl groups: influence of surface group topology from nonlinear oscillatory shear. Langmuir 39(18):6433–6446. https://doi.org/10.1021/acs.langmuir.3c00210